Micro and Nanostructures 194 (2024) 207940

Contents lists available at ScienceDirect

Micro and Nanostructures

journal homepage: www.journals.elsevier.com/micro-and-nanostructures

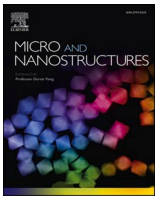

A new $CsPbI_2Br$/CuZnSnSSe/Si tandem solar cell with higher than 32 % efficiency

Naceur Selmane [a,*], Ali Cheknane [a,**], Hikmat S. Hilal [b,***]

[a] Materials Lab, Energetic Systems, Reneauable Energies and Managemant, (LMSEERGE). University of Amar Telidji-Laghouat. Boulevard of Martyrs BP37G, Laghouat, 03000, Algeria
[b] SSERL, Chemistry, College of Sciences, An-Najah N. University, Nablus, P400, Palestine

ARTICLE INFO

Keywords:
Tandem solar cells
$CsPbI_2Br$ perovskite
Simulation
SCAPS
CZTSSe/Si

ABSTRACT

To avoid Shockley-Queisser limit in single p-n junctions, tandem solar cells were proposed. A new tandem cell is simulated here using the 1-dimensional SCAPS. The new cell combines two reported single solar cells together, aiming at achieving high performance by optimizing various layer characteristics. The bottom sub-cell is Mo/Si(p)/CZTSSe(p)/CdS(n)/ZnO(i)/ZnO(Al), where ZnO is an electrodeposited transparent-conductor oxide, with high UV transmittance, ZnO(i) is intrinsic layer, CZTSSe/Si is bi-absorber layer of p-CuZnSnSSe and p-Si, Mo is back contact. The optimized sub-cell exhibits a high fill factor of 85.18 % with overall efficiency 20 %. Based on literature, a perovskite $CsPbI_2Br$ layer is included in the top sub-cell Cu_2O(HTL)/$CsPbI_2Br$)/TiO_2(ETL), where Cu_2O is a hole-transport layer and TiO_2 is electron-transport layer. The top sub-cell layers have been carefully selected for best alignment. Matching and optimizing various parameters in the two sub-cells is a simulation challenge. Therefore, layers in the two sub-cells have been studied separately, keeping in mind the proper combinations between various layers. With optimized layer thicknesses and band gaps, together with proper alignment of band edges, the proposed tandem solar cell exhibits high characteristics of 80 % fill factor and higher than 32 % overall efficiency.

1. Introduction

Solar cells, being among the major tools to utilize the clean solar energy, have witnessed tremendous research and development. Solar cells first started with single junctions involving Si [1] or other materials such as CdTe [2] and Ge [3]. Nowadays, Si solar cells show efficiencies of 25 % [4,5]. Solar cells further progressed through various generations, each of which exhibited higher stability and performance at lower cost. Second generation solar cells, based on amorphous silicon, CdTe and CuInGaSe (CIGS), exhibited efficiencies of higher than 9, 20 and 23 %, respectively [6]. Third generation solar cells based on perovskites are also known [6–8] with soundly good performance. Perovskites have the advantages of suitably wide gaps and high absorption coefficients [9,10], in addition to high charge-carrier mobility, thermal stability, long life span and ease of manufacturing [11,12]. $CsPbI_2Br$ perovskite shortcomings were studied to improve its performance by various modifications [13–15].

* Corresponding author.
** Corresponding author.
*** Corresponding author.
E-mail addresses: n.selmane@lagh-univ.dz (N. Selmane), a.cheknane@mail.lagh-univ.dz (A. Cheknane), hshilal@najah.edu (H.S. Hilal).

https://doi.org/10.1016/j.micrna.2024.207940
Received 3 May 2024; Received in revised form 23 June 2024; Accepted 24 July 2024
Available online 2 August 2024

Despite earlier achievements, single junction solar cells still suffer the Shockley-Queisser limitation (30 %) in single junctions [11,16–18]. To overcome this limitation, tandem cells were considered [9] with success, given that tandem cells consist of multiples sub-cells stackings together [19]. Various materials are involved in tandem cells including perovskites [20–23].

In the present study, a new tandem solar cell is proposed. It is based on a perovskite $CsPbI_2Br$ layer in the top sub-cell [24,25] and the CZTSSe/Si double absorber layer in the bottom sub-cell. The main assumptions to be tested are: 1) The materials have special features as reported earlier for separate solar cells. 2) The perovskite has a good absorption coefficient which should yield high cell performance. 3) Combining between $CsPbI_2Br$ with CZTSSe sub-cells should yield a tandem cell with improved performance once optimized layer characteristics are well matched and optimized. 4) Inclusion of the Si in the double absorber layer CZTSSe/Si should widen the absorption spectrum in the bottom sub-cell and improve the cell performance. All these assumptions will be tested here.

Although the bottom sub-cell involves the environmentally questionable Pb element, it is still widely considered in solar cell research due to its stability [26–28]. Its environmental impact is being minimized by using thinner layers. On the other hand, the CZTSSe/Si layer involves safe, environmentally friendly, stable and low-cost constituents, with a wide absorption range. The CZTSSe itself is widely used in solar cells [29,30].

The simulation involves thicknesses of both sub-cell layers together with their band gap values. Matching between the perovskite and CZTSSe layers are optimized. To our knowledge, combining these materials ($CsPbI_2Br$ with CZTSSe/Si) in a tandem solar was not reported earlier, which highlights novelty of the present study. In fact, other closely related tandem cells, such as those involving $CsPbI_2Br$ and CZTSSe, were reported [31] but with double absorber layer. Using the double absorber layer CZTSSe/Si is not arbitrary here. The Si has a narrow gap while CZTSSe band gap is wider. This allows cultivation of photons with wider wavelength range in the bottom sub-cell. Matching various parameters (thickness, band gap and doping concentration) between the two absorber layers, to enhance performance was not described before.

Experimental results for the TCO and ZnO layer, and other literature values, are included in the present simulation study. In separate cells of CZTSSe/Si about 20 % efficiency was earlier reported [32,33]. When used as a bottom sub-cell here, higher efficiency can be achieved by optimizing the layer parameters as described here. Moreover, by adding the top sub-cell, an improved efficiency of higher than 32 % can be reached here.

To avoid extra costs associated with experimental works, researchers use simulation study to predict the behaviors of solar cell components [34–36]. Many studies on solar cells used the TCAD Silvaco [37,38], Afors program [34], the Comsol [39] and AMPS [40]. Other studies used the SCAPS program that proved to be a powerful software [41–45] and is being used here.

The present simulation study is conducted stepwise. An in-depth investigation is conducted to optimize some the bottom sub-cell layer physical properties through a series of carefully designed calculations. Layer thickness, doping concentration and band gap have been systematically varied while keeping all other factors fixed. Simultaneously, the parameters of the CdS layer (thickness, band gap and doping concentration) were also optimized, keeping other layers fixed. This approach allows for a comprehensive analysis of the CdS emitter layer and its impact on the tandem solar cell overall performance. The resulting data have then been analyzed, using contour profiles and heat maps. These graphical representations provided valuable insights into the intricate interplay between different parameters and their influence on the performance characteristics of both the CZTSSe and perovskite layers. Another issue with CdS is its hazardous nature, as described my its MSDS information. Despite its hazardous nature, it is being widely used in solar cells [46–48]. Minimizing the hazards of CdS is being considered. One strategy is to use minimal CdS layer thickness. Stabilizing the solar cell is another important strategy to avoid environmental contamination with Cd ions. Moreover, research is active to recycle solar cells that involve CdS and to avoid environmental contamination [49,50]. Replacing the CdS layers with other safer materials, such as Ag BaTiSe [51], ZnS [52] or SnS [53] was also reported. Using a thin CdS layer here is necessary to make comparison with earlier literature as shown in Table 4 below.

The simulation results yield a comprehensive understanding of the optimal parameters for the tandem solar cell. Identification of the precise combination of layer-thicknesses, band-gaps and doping-concentrations, to exhibit highest tandem cell performance, is described. The protocols followed here will induce further advancement in renewable energy technology.

Table 1
Major layer parameters in the bottom sub-cell based on literature [64,80,81].

Property	Layer				
	Si	CZTSSe	CdS	i-ZnO	ZnO(Al)
Thickness (nm)	1000	Variable	40	100	150
Bandgap E_g (Ev)	1.12	Variable	2.600	3.370	3.370
Electronic affinity χ (eV)	4.05	4.100	3.750	4	4
Dielectric permittivity ∈ r (relative)	11.68	7	8.730	9	9
Density of states of conduction band DOS. CB (cm^{-3})	2.82×10^{19}	2.2×10^{18}	3.3×10^{18}	3.6×10^{18}	3.6×10^{18}
Density of states of valence band DOS. VB (cm^{-3})	1.83×10^{19}	7x10*19	1.36×10^{19}	1.13×10^{19}	1.13×10^{19}
Electron thermal					
Velocity (cm/s)	1×10^7	1×10^7	1×10^7	1×10^7	1×10^7
Hole thermal velocity (cm/s)	1×10^7	1×10^7	1×10^7	1×10^7	1×10^7
Electron mobility (cm^2/Vs)	1100	100	160	150	150
Hole mobility (cm^2/Vs)	420	35	15	50	50
Donor density ND (cm^{-3})	–	–	1×10^{17}	–	8×10^{18}
Acceptor density, N_A (cm^{-3})	10^{19}	Variable	–	–	–
Defect type (cm^{-3})	Neutral variable	Neutral variable	1×10^{15}	1×10^{16}	1×10^{16}

Table 2
The bottom layer defects used in SCAPS-1D.

Properties	Defect type	Total Density (N_t)	Capture cross section electrons (cm^2)	Capture cross section holes (cm^2)	Energetic distribution	Energy level with respect to reference
p-Si	SCAPS model	SCAPS model	SCAPS model	SCAPS model	SCAPS model	SCAPS model
p-CZTS	Donor	1×10^{14}	5×10^{-13}	1×10^{-15}	single	0.1–0.4 eV
	Acceptor	5×10^{14}	1×10^{-15}	1×10^{-15}	single	0.5–0.3eV
n-CdS	SCAPS model	SCAPS model	SCAPS model	SCAPS model	SCAPS model	SCAPS model
n-ZnO	SCAPS model	SCAPS model	SCAPS model	SCAPS model	SCAPS model	SCAPS model
CZTSSe/CdS	Neutral	1×10^{12}	1×10^{-14}	1×10^{-14}	uniform	0.6

Table 3
Major layer parameters for the top sub-cell used in SCAPS-1D [82].

	Layer		
Property	TiO_2 (ETL)	$CsPbI_2Br$	Cu_2O (HTL)
Thickness (μm)	0.04	1	0.250
Bandgap (eV)	3.2	1.5	2.170
Affinity (eV)	3.9	3.7	3.200
Dielec. Perm	9	8.6	7.11
Density of states in conduction band DOS CB (cm^{-3})	1×10^{21}	1.9×10^{19}	2.02×10^{17}
Density of states in valence band DOS VB (cm^{-3})	2×10^{20}	2.37×10^{20}	1.1×10^{19}
Electron mobility μe (cm^2/Vs)	20	25	200
Hole mobility μh (cm^2/Vs)	10	25	80
Donor concentration Nd (cm^{-3})	2×10^{-19}	–	–
Acceptor Concentration Na (cm^{-3})	–	1×10^{15}	1×10^{18}
Absorption	–	SCAPS model	SCAPS model
Nt defect (cm^{-3})	3.6×10^{16}	1×10^{17}	1×10^{17}

Table 4
Summary of characteristics for tandem solar cell and separate bottom sub-cell.

Entry No.	Structure	V_{OC} (V)	J_{SC} (mA/cm^2)	*FF* (%)	η (%)	Ref.
1	Bottom layer Sub-Cell with (CZTSSe/Si absorber)	0.742	37.18	85.18	20.94	This work
2	Top sub-cell with $CsPbI_2Br$	1.06	27.4	83 %	11.51	This work
3	Tandem with both CZTSSe/Si and $CsPbI_2Br$ perovskite	1.81	27.79	79.89	32.41	This work
4	"CZTS/PSC/CZTS/CdS/ZnO/FTO"	1.18	24.7	88.36 %	25.95 %	[21]
5	$CsPbI_3$/CZTSSe tandem solar (four-terminal solar cell)	1.5	15.75	87	32.35 %	[31]
6	Perovskite/CIGS tandem	2.01	19.9	80	32	[101]
7	Perovskite-CIGS Monolithic Tandem Solar Cells	1.92	20.04	77 %	29.7	[102]
8	Perovskite and CIGS Tandem Solar Cell	2.25	25.8	73.02	30.71	[103]
10	(FTO/ETL/$CH_3NH_3SnI_3$/HTL/Back contact)	1.12	29.44	88.82	29.24	[104]
11	Glass/TCO/TiO_2/$CZTSe_{1-x}S_x$/$CH_3NH_3SnI_3$/Back contact	0.85	29.22	70.47	17.57	[105]
12	Spiro-OMeTAD/$CH_3NH_3PbI_3$−xCIx (without ETM)/CIGS	1.23	28	80.71	27.74	[105]

2. Materials and methods

The Al-doped ZnO films have been prepared as described by literature [54,55]. Details of preparation are described in Supplementary Sections S2.1-2.3.

The prepared ZnO films have been characterized by transmittance spectra, X-ray diffraction, scanning electron microscopy as described in Supplementary Section 2.4. Supplementary Figs. S1–S3 confirm the nature of the prepared films, by comparison with literature [56–64].

2.1. Structure description and simulation details

In this study, the SCAPS program, an excellent 1-dimensional program for simulating heterojunction cells, has been used. The SCAPS predicts the electrical behaviours for most semiconductors and structures. It is based on differential equations such as: Poisson and continuity equations (Equations (1) and (2)) [65–67] together with transport of holes and electrons (Equation (3)) [68,69],

$$\frac{d^2}{dx}\phi(x) = \frac{q}{\varepsilon_o \varepsilon_r}(p(x) - n(x) + N_D + N_A + \rho_p - \rho_n) \quad (1)$$

$$\frac{\partial J_p}{\partial x} - R_p + G_p = \frac{\partial p}{\partial x} \quad (2a)$$

$$\frac{\partial J_n}{\partial x} - R_n + G_n = \frac{\partial n}{\partial t} \quad (2b)$$

$$J_n = q\mu_n E_n + qD_n d_n \quad (3a)$$

$$J_p = q\mu_p E_p + qD_p d_p \quad (3b)$$

$$D_p = \frac{kT}{q}\mu_p, D_n = \frac{kT}{q}\mu_n \quad (3c)$$

where J_p & J_n are current densities of holes and electrons, respectively. ϕ is potential, ε_o and ε_r are the vacuum and relative permittivity, q is elementary charge, N_D & N_A are donor & acceptor impurity atom concentrations that are the same with ionized atoms at room temperature, the difference ρ_p-ρ_n corresponds to the density of deep defect centers [70,71], R_n, G_n recombination and generation rates of electrons, respectively, R_p, G_p are recombination and generation rates for holes, respectively. The D_n, μ_n, D_p, μ_p represent diffusion coefficients and mobility of electrons and holes, respectively. The relation between the two coefficients is the Einstein relation (Equation number 3.c) [72,73], where k is the Boltzmann constant, T is the Kelvin temperature and q is the electron charge.

The simulated structure includes two sub-cells. The bottom sub-cell involves Mo/Si(p)/CZTSSe(p)/CdS(n)/ZnO(i)/ZnO(Al) where the ZnO(Al) is a transparent conductor oxide, and ZnO is an intrinsic layer. CdS is an n-doped emitter layer that formulates the heterojunction with the double absorber p-Si/p-CZTSSe. The inclusion of CZTSSe is to improve absorption of incident photons. The back contact is the molybdenum (Mo). The top sub-cell involves precise layers each for a specific purpose, namely Cu_2O(HTL)/$CsPbI_2Br$)/TiO_2(ETL), where TiO_2(ETL) is the electron-transport layer [74], $CsPbI_2Br$ is the inorganic perovskite [15] and the hole-transport layer is Cu_2O(HTL) [75]. The tandem structure which combines the top and the bottom sub-cells is summarized as Mo/Si(p)/CZTSSe(p)/CdS(n)/ZnO(i)/ZnO(Al)/Cu_2O(HTL)/$CsPbI_2Br$)/TiO_2(ETL), Fig. 1. All physical and geometric properties of layers are based on the present experimental results (described in the Supplementary Materials) and earlier works described in Tables 1 and 2 The Tables show layer thicknesses, band gaps, doping concentrations together with defect densities and interfaces. Controlling defect density is necessary for cell performance improvement, and should be carefully made. Otherwise, the defect value may affect the layer type itself, or may reverse the population type at the interface that may change the electrical behaviour of the structure. The CZTSSe/CdS interface is taken of neutral type with uniformly distributed estimated density 1×10^{12} cm^{-3}. The same remark applies to other structure layers CZTS, CdS, ZnO and Si, in the bottom sub-cell. The TiO_2(ETL), Cu_2O(HTL) and $CsPbI_2Br$ layer properties and defects of the top sub-cell are described in Table 3. The layer defect types and densities are kept fixed, while thicknesses, doping

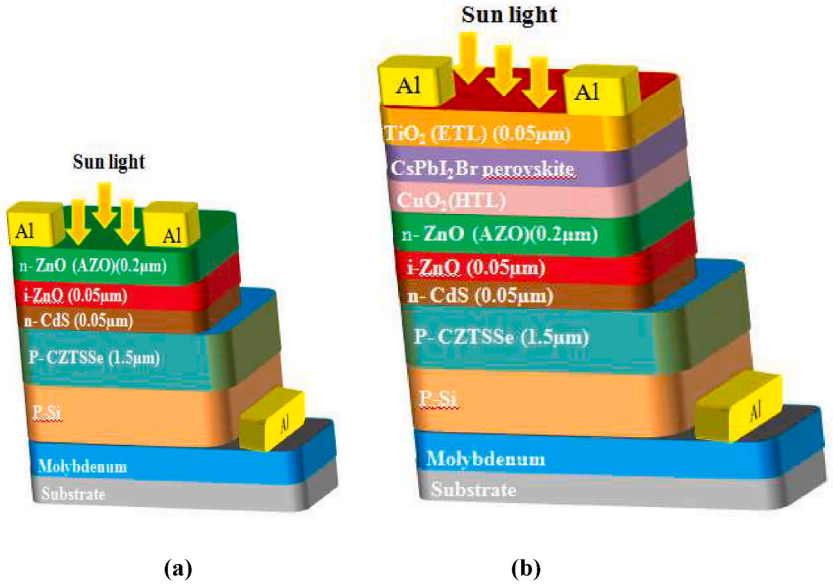

Fig. 1. Schematic showing proposed solar cell structures with double absorber layer CZTSSe/Si for (a) separate bottom sub-cell, and (b) tandem solar-cell.

concentrations and band gaps are varied for optimization, while carefully matching the bottom and top sub-cells. In simulations, the incident power density used here is 1000 mW/cm^{-2} with AM 1.5 spectrum.

The front aluminum-doped zinc oxide layer, denoted as ZnO(Al) or AZO, which is electrochemically prepared, is added at the top of the bottom sub-cell in its separate state. The ZnO(Al) layer, considered as a window for incident photons, is important as it combines between transparency and conductivity. The transparency is due to the wide band gap (~3.3 eV), while the high conductivity (reported from 20 to 1000 $\Omega^{-1}cm^{-1}$) depending on concentration, is ensured by the aluminum doping, based on literature [76–78].

Next, is the n-CdS emitter layer, with a wide band gap of 2.6 eV [79], to form the junction with the p-CZTSSe layer. Both p-CZTSSe and p-Si layers together form a double absorber layer, to improve the solar cell performance. The double absorber layer is responsible for photon absorption in a wider range to generate more electron-hole pairs, and is expected to yield higher photo generated current. Finally, the Mo back contact collects the holes that go to the external circuit, Fig. 1.

3. Results and discussions

3.1. Effects of bottom sub-cell layer parameters

Some physical parameters of bottom sub-cell important layers, CZTSSe and CdS, are studied together to see the effects on the solar cell performance. The studied parameters are: thickness, doping level and band gap. Other parameters are kept fixed, including Si layer thickness and doping concentration.

3.1.1. Effect of CZTSSe layer thickness

CZTSSe layer thickness effect on the performance of the bottom sub-cell Mo/Si(p)/CZTSSe(p)/CdS(n)/ZnO(i)/ZnO(Al) has been studied. The thickness varies from 1 to 2 μm with Si layer thickness fixed at 1 μm. Other parameters are kept constant, as outlined in Table 1.

As expected, layer thickness affects cell performance, by affecting other phenomena, such as diffusion length. With increased p-CZTSSe layer thickness, Fig. 2b, open-circuit potential V_{OC} increases from 0.61 to 0.71 V, and short-circuit current density J_{SC} increases from 28.7 to 36.3 mA/cm^2. The J_{SC} increase is justified by the increased photon absorption with higher thickness, which leads to generation of more electron-hole pairs, and consequently increased J_{SC}.

Moreover, the increased p-CZTSSe layer thickness to an extent, lowers the recombination probability. That is because larger space for charge carriers allows more opportunity for diffusion without encountering recombination. Consequently, V_{OC} increases.

Similar logic applies to fill factor and efficiency improvement. *FF* increases from 76.7 to 84.2 % by increasing CZTSSe layer thickness from 1 to 2 μm. With higher J_{SC}, V_{OC} and *FF* values, the conversion efficiency increases from ~13.5 % to ~18.4 %, as described in Fig. 2a.

Despite the findings, the CZTSSe layer thickness should not be too high, for more than one reason. Firstly, to avoid reversible effects associated with possible trap formation that may increase recombination. Secondly, to avoid photon screening of the Si layer when using a thick CZTSSe layer, as the wider band gap CZTSSe is a window for the narrower band gap Si layer.

3.1.2. CZTSSe layer doping concentration effect

Keeping the CZTSSe layer thickness at optimal value 2 μm, and the Si layer at 1 μm, the CZTSSe doping concentration is varied from 1×10^{15} to 1×10^{18} cm^{-3}. All other parameters are kept fixed. Effects of varying the CZTSSe doping concentration, on cell performance, are summarized in Fig. 3. Fig. 3a summarizes photo-current density vs applied bias (*J-V*) plots for various layer concentrations. Fig. 3b shows that the cell efficiency increases with increasing doping concentration up to a maximum value 19.07 % at 1×10^{17} cm^{-3} concentration. With increased doping concentration, the conductivity and charge carrier transportation increase yielding higher current density [83]. This is observed by the J_{SC} maximum value 36.9 mA/cm^2 at the 1×10^{17} cm^{-3} concentration, Fig. 3c. The improvement in charge carrier transport increases the *FF* value, with a maximum value 81.4 % at 1×10^{17} cm^{-3} concentration, Fig. 3b.

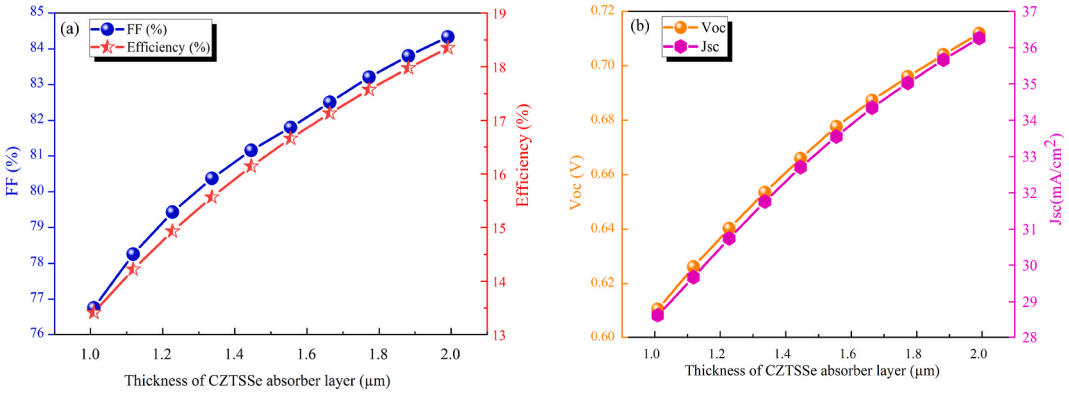

Fig. 2. CZTSSe layer thickness effect on bottom sub-cell characteristics. (a) η% & *FF*%, (b) J_{SC} and V_{OC}.

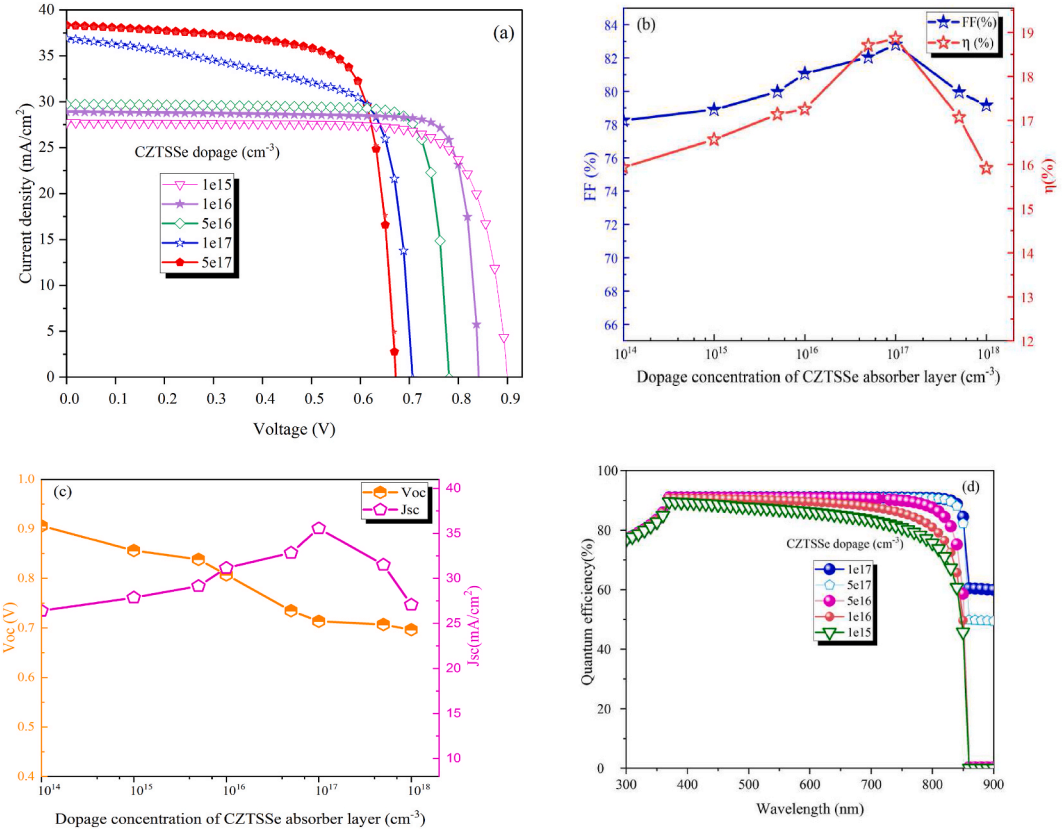

Fig. 3. CZTSSe layer doping concentration effect on bottom sub-cell performance. (a) *J-V* plots, (b) *η*% & *FF*%, (c) J_{SC} & V_{OC}, (d) Quantum efficiency variation with wavelength.

The V_{OC} value decreases to 0.71 V, as expected with increased doping concentration, but the overall efficiency is compensated for by the increased current density and fill factor values.

Excessive doping concentration, at higher than 1×10^{17} cm^{-3}, shows negative effect on the cell performance. This is understandable, as higher concentration leads to higher defect density and more trap formation that encourage recombination. This is clearly observed in J_{SC} significant lowering at concentrations higher than 1×10^{17} cm^{-3}. On the other hand, the value for V_{OC} remains the same or slightly lower.

The Si layer doping concentration is kept constant at 10^{19} cm^{-3}, and higher than the CZTSSe layer. The doping concentration difference makes depletion region extend in the side of CZTSSe which is important to create a high electric field at the CZTSSe/Si interface [84]. This helps in charge carrier separation. Same logic applies to the CZTSSe/CdS interface as well, *vide infra*.

Fig. 3d shows that the quantum efficiency value systematically increases with increased CZTSSe doping concentration from 1×10^{15} to 1×10^{17} cm^{-3}. The wavelength range is also further expanded to the infra-red range. It can be noted that further increase in doping concentration from 1×10^{17} to 5×10^{17} cm^{-3} yields only modest increase in quantum efficiency.

3.1.3. CZTSSe layer band gap effect

The CZTSSe layer band gap value is another major parameter to study, as it may affect the cell performance. The band gap controls the light absorption behavior. Normally, high absorption coefficient covering most incident photons, in the visible and near inferred wavelengths, is favored. In the present study, the CZTSSe layer band gap value has been varied in the range 1.00–1.50 eV, while fixing the Si layer band gap at 1.12 eV. The results are summarized in Fig. 4.

Larger CZTSSe band gap yields a higher V_{OC}, Fig. 4c. That is understandable as a larger band gap creates a higher energy barrier, preventing charge carriers from easy passage [85]. As a result, the charge carriers experience enhanced separation and reduced recombination, leading to a higher V_{OC}.

J_{SC} value increases, with increased bandgap, until a maximum value 37.1 mA/cm^2 is observed at band gap 1.40 eV, Fig. 4c. Similarly, *FF* exhibits a maximum value of 84.7 % at the same doping concentration, Fig. 4b. The bottom sub-cell exhibits a maximum conversion efficiency 20.23 at CZTSSe band gap value 1.40 eV, Fig. 4b.

With band gap larger than 1.40 eV, the cell parameters J_{SC}, FF and conversion efficiency all decrease. Only V_{OC} remains nearly constant at higher band gap values. At a very high band gap, the photocurrent is lowered due to increased recombination in the absorber layer, and lowered probability to create electron-hole pairs. Higher band gap does not allow absorption of photons with lower

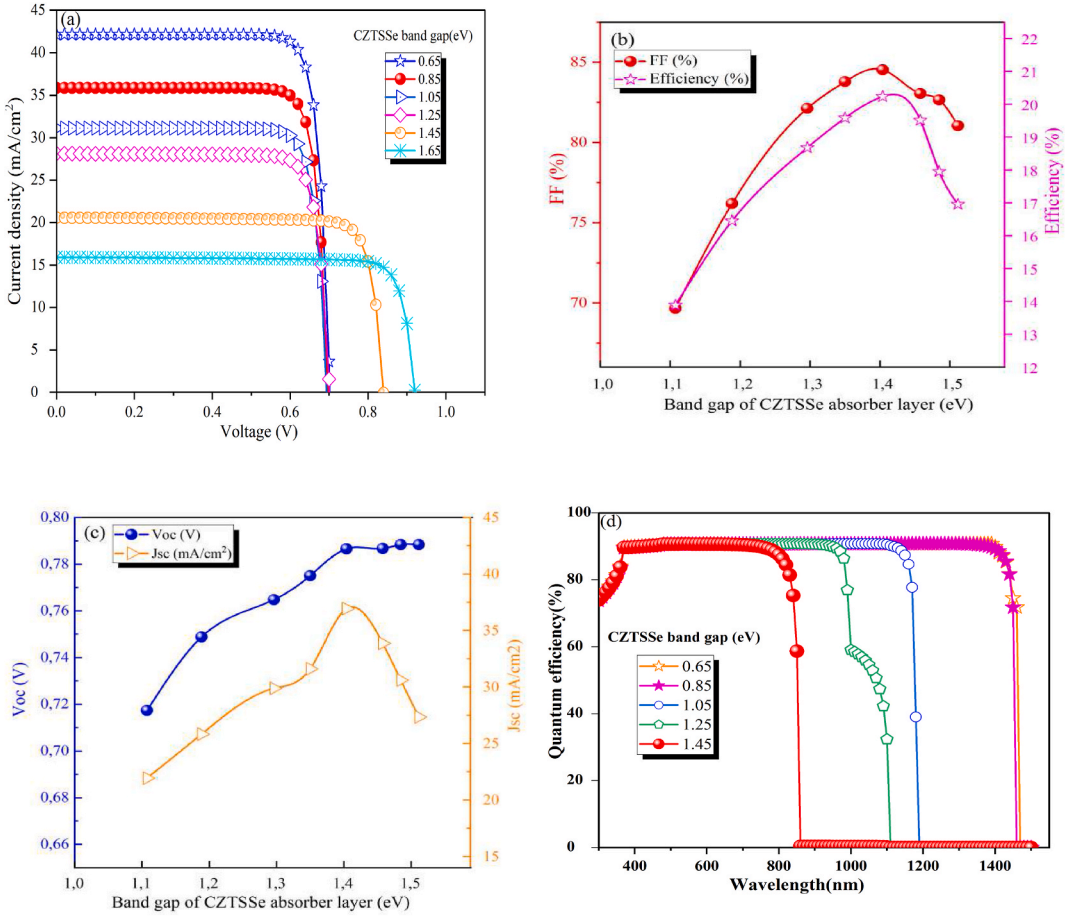

Fig. 4. CZTSSe layer band gap variation effect on bottom sub-cell performance. (a) *J-V* plots, (b) *η*% & *FF*%, (c) J_{SC} & V_{OC}, (d) Quantum efficiency variation with wavelength.

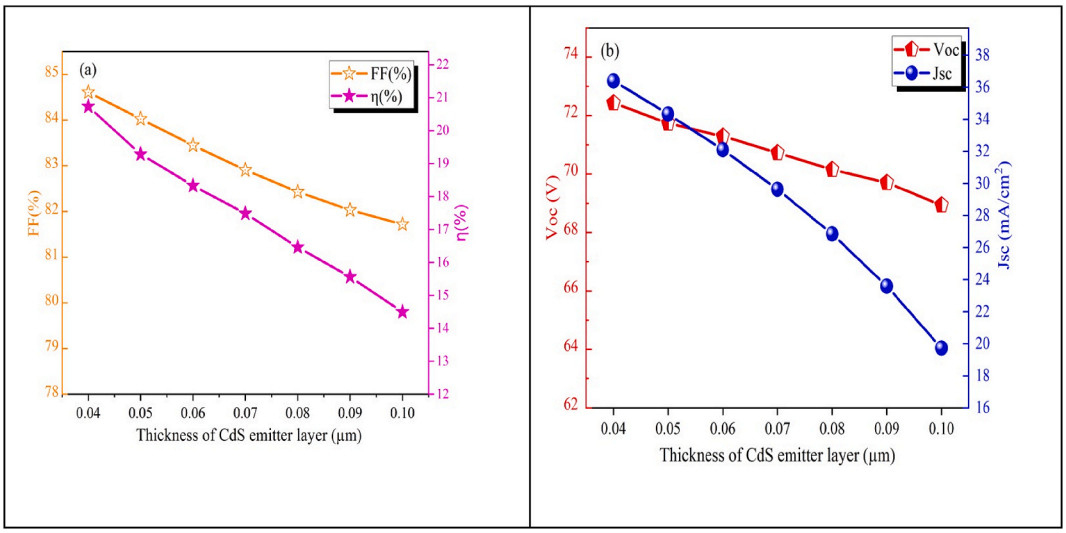

Fig. 5. CdS emitter layer thickness effect on bottom sub-cell performance. (a) *η*% & *FF*%, (b) J_{SC} & V_{OC}.

energy [86]. Naturally, J_{SC} and other cell parameters such as efficiency and *FF* are lowered.

Therefore, an optimal CZTSSe band gap 1.40 eV ensures highest *FF* and efficiency, Fig. 4b. The need for the Si layer with band gap 1.12 eV is also justified. The Si behaves as a bridge that permits the free passage of hole carriers to the back contact (Mo). With no Si layer, the work functions of the interface CZTS/Mo are 5.32 and 4.80 eV respectively, with a built potential of 0.52 eV. The Si layer bridge lowers the potential difference value to obtain a band gap alignment or a flat band mode. Furthermore, the graded band gaps of CZTSSe and Si layers maximize the absorption and generate more hole-electron pairs. The bi-absorber layer covers the entire visible radiations, as the CZTSSe layer covers the shorter wavelengths and the Si layer covers the longer wavelengths [87]. The result is more photon absorption.

3.1.4. CdS emitter-layer thickness effect

The n-CdS layer complements the junction formation with CZTSSe absorber layer. Its physical parameters should thus be optimized. The CdS layer thickness is carefully chosen in the range 0.04–0.10 μm, based on earlier literature [88,89]. Earlier studies used a layer thickness range 0.04 and 0.05 μm [89,90]. The idea was to make charge-carrier life time longer, by making diffusion length greater than the layer thickness, to ensure free passage to the contacts. The simulation results corroborate this logic. Fig. 5 shows that all cell performance characteristics decrease with increased CdS layer thickness. Among various thicknesses, 0.04 μm exhibits highest efficiency of 20.67 % and *FF* 84.6 %, Fig. 5a, in congruence with literature [90,91]. Same behavior is observed for J_{SC} and V_{OC} as shown in Fig. 5b.

3.1.5. CdS layer doping concentration effect

Effect of varying CdS doping concentration on bottom sub-cell performance is described in Fig. 6. From the Figure, all cell characteristics (efficiency, *FF*, J_{SC} and V_{OC}) increase with concentration up to a limit ($\sim 1 \times 10^{17}$ cm^{-3}). At higher concentrations, all characteristics decrease.

Higher doping concentration leads to improved conductivity and charge carrier mobility. This increased mobility contributes to higher J_{SC} values. Similarly, for V_{OC} the optimal concentration allows better energy level alignment at the n-CdS/p-CZTSSe interfaces, with minimal band discontinuity caused by band gap difference.

The findings indicate that higher doping concentrations effectively lower recombination rates by passivating trap states. This leads to improved *FF* and efficiency (η). Consequently, the global current level in the *J-V* curve increases with higher CdS doping concentrations. However, all such improvements occur but to a certain concentration level. After that, the CdS layer is subjected to more imperfections and traps that lower J_{SC} and other characteristics.

3.2. The tandem solar cell

Having studied the bottom sub-cell, it is time to investigate the complete tandem solar cell as a whole. An in-depth analysis, using contour profile approach, to thoroughly investigate and understand the intricate effects of manipulating thickness and band gap for the tandem solar cell layers, is presented. The objective is to optimize these parameters in order to maximize performance of the proposed tandem cell. Heat maps are two-dimensional representations of data, where colors represent the values. Heat maps help understand complex data sets. Color representation is the easiest way to present the data and to correlate data values, as proposed earlier [40]. The change from blue to red indicates increased performance. Contour plots are also graphical presentations for 3-dimensional surfaces, by drawing constant z-slices (contours) on two-dimensional formats. Thus, at a given z value, lines connecting the (x,y) coordinates are drawn [41].

The focus here is on the top sub-cell involving Cu_2O(HTL), $CsPbI_2Br$ (active layer) and TiO_2(ETL), using optimized parameters simulated for the bottom sub-cell described in Section 3.1 above.

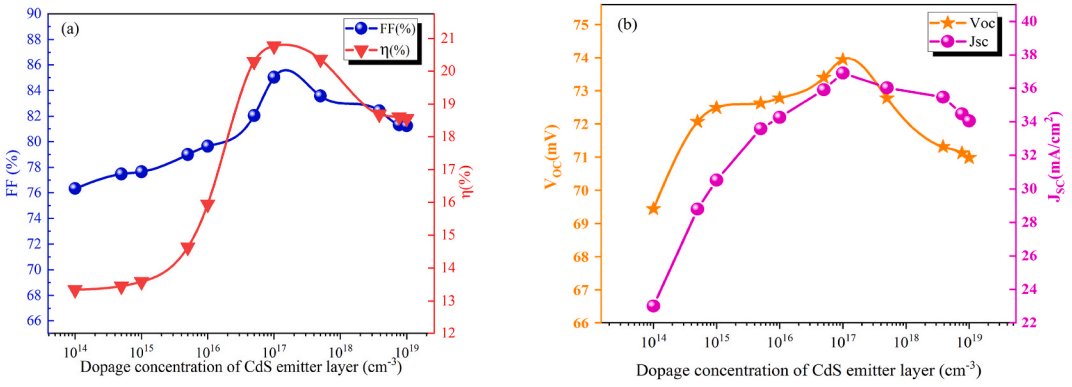

Fig. 6. CdS emitter-layer doping concentration effect on bottom sub-cell performance. (a) η% & *FF*%, (b) J_{SC} & V_{OC}.

3.2.1. CZTSSe and $CsPbI_2Br$ perovskite layer thickness effects

Layer thicknesses for both CZTSSe and $CsPbI_2Br$ perovskite are varied simultaneously. That is to ensure calculation accuracy and minimize errors associated with calculations made separately. The CZTSSe layer thickness is varied from 1.1 to 2.2 μm, while the $CsPbI_2Br$ layer thickness is varied between 0.1 and 1.2 μm. Relatively wide ranges are used to find optimized values. For the CZTSSe layer, the values are based on bottom sub-cell thicknesses described above. For the perovskite (top sub-cell), small layer thicknesses are chosen to avoid any photon screening. All other parameters are kept fixed. By progressively increasing the thicknesses of both CZTSSe and $CsPbI_2Br$ perovskite layers, within the tandem solar cell, the cell characteristics initially increase, as observed from varying colors in Fig. 7. With thicker CZTSSe and $CsPbI_2Br$ perovskite layers, higher absorption of photons occurs. Thus, a higher number of electron-hole pairs are generated, leading to an increased J_{SC} as observed in Fig. 7e and f.

Maximum values of efficiency (>30 %) and *FF* (>81 %) correspond to layer thickness combination of 1.8 and 0.9 μm for CZTSSe and perovskite, respectively, as shown in Fig. 7a–d. The highest J_{SC} and V_{OC} values, 27.7 mA/cm^2 and 1.81 V, respectively, occur at the same layer thickness combination, Fig. 7e–h. One may question why the optimal combination occurs using thinner perovskite (0.9 μm) than CZTSSe (1.8 μm). This is because the perovskite is placed at the top, and being thinner prevents photon screening away from the CZTSSe layer.

As described above, thick absorber layers enable more absorption and higher number of electron-hole generation, leading to higher J_{SC}, as reported earlier [92]. On the other hand, too high thickness values cause more recombination that lowers J_{SC}, *FF* and η.

It should be noted that the maximum J_{SC} for the tandem cell ~27 mA/cm^2, at optimal thicknesses, is smaller than the value for the separate bottom sub-cell ~37 mA/cm^2. This is not unexpected, as the two sub-cells in the tandem structure are connected in-series, and the total current is determined by the smaller one. On the other side, the maximum V_{OC} for tandem cell, at optimal thickness values, is 1.81 V, which is nearly the summation of V_{OC} value 0.80 V for bottom sub-cell and 1.00 V for top sub-cell.

3.2.2. CZTSSe and $CsPbI_2Br$ perovskite band gap effects

Band gaps affect the tandem cell performance. The present structure involves a larger band gap for $CsPbI_2Br$ perovskite layer that absorbs shorter wavelengths, and allows passage of longer wavelength photons towards the bottom sub-cell absorbers [93]. In the

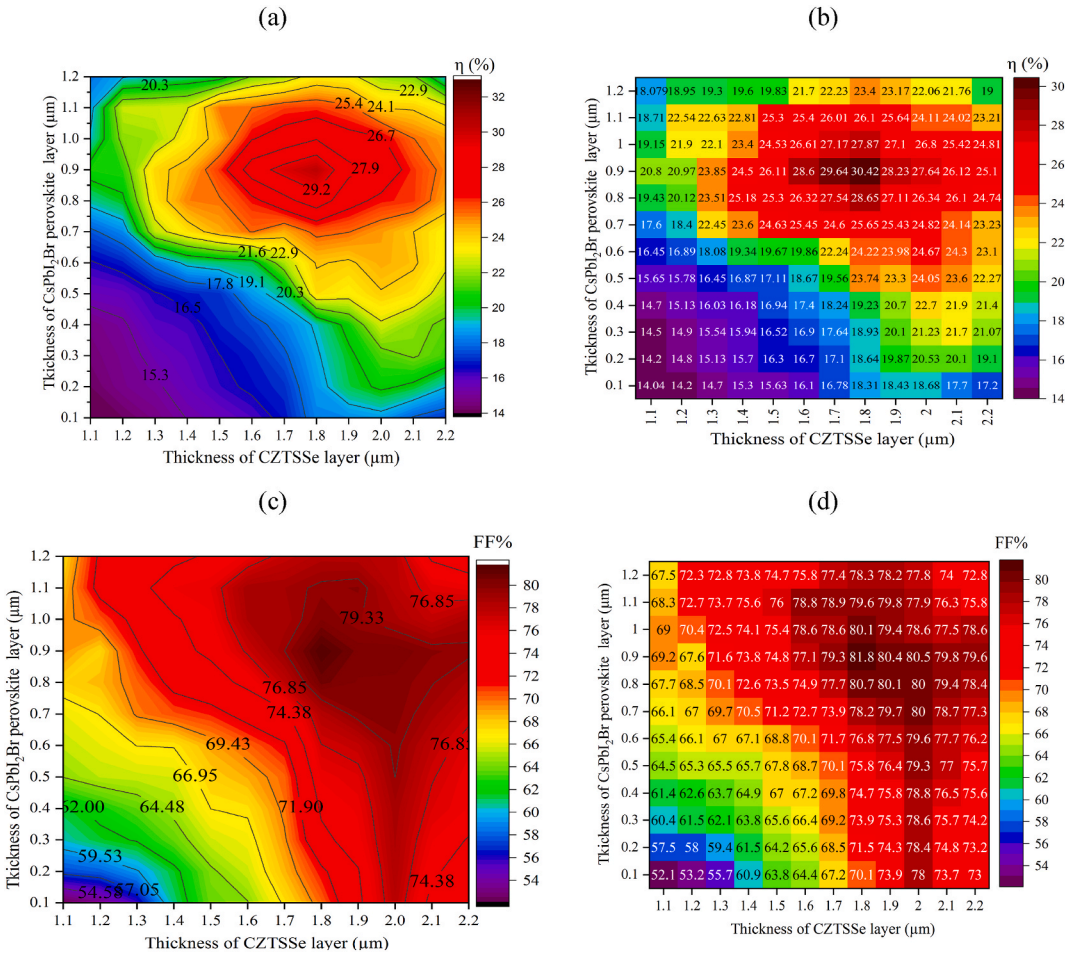

Fig. 7. CZTSSe and $CsPbI_2Br$ thickness effects on tandem solar cell characteristics. (a) & (b) for η%, (c) & (d) *FF*%, (e) & (f) J_{SC}, (g) & (h) V_{OC}.

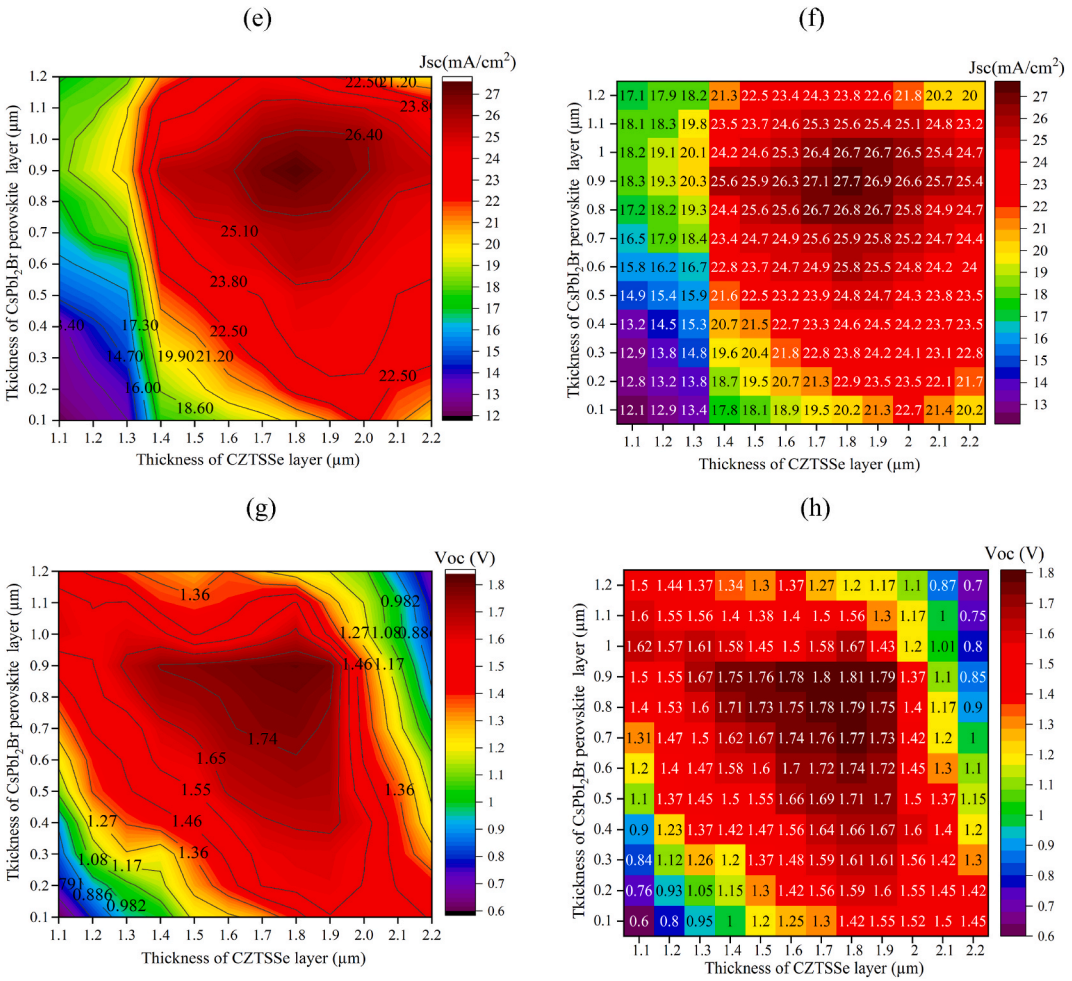

Fig. 7. (*continued*).

present study, effects of band gaps of both CZTSSe and $CsPbI_2Br$ perovskite layers have been studied, as described in Fig. 8. In the simulation, band gap values in the ranges 1.00–1.50 and 1.40–1.90 eV for CZTSSe and perovskite, respectively, are used. The optimal layer thicknesses observed from Fig. 7, namely 1.8 and 0.9 μm for CZTSSe and perovskite, respectively, are used. Again, the perovskite layer thickness is being lower than that for CZTSSe layer [94], as discussed above.

At the beginning, increasing band gaps of both layers, CZTSSe and $CsPbI_2Br$ perovskite, increases the efficiency values from 20 to 21 % (in blue color) to 22–23 % (in yellow color) till the highest value 32.27 % is achieved, Fig. 8a. The 1.40 and 1.65 eV band gaps for CZTSSe and $CsPbI_2Br$, respectively, show the optimal combination. Highest characteristics, expressed as efficiency (32.27 %), J_{SC} (27.4 mA/cm^2), *FF* (81.8 %) and V_{OC} (1.81 V), are observed at these band gap values, Fig. 8a–h. A wider band gap typically results in a higher V_{OC} value [95], by enabling larger built-in potential and reducing recombination [96]. The Figure shows also that higher efficiency values are achievable when the band gap for the perovskite is wider than for CZTSSe, in congruence with literature [94] as described above.

The relatively wide band gap (1.65 eV) for $CsPbI_2Br$ is useful in the $CsPbI_2Br/TiO_2$ and $CsPbI_2Br/Cu_2O$ (HTL) interfaces. The discontinuity between the $CsPbI_2Br$ and the hole transport layer Cu_2O(HTL) is lowered which allows a free passage for the holes with no difficulty. Hole transport layers are normally carefully chosen based on that in perovskite solar cells [97]. The perovskite conduction-band energy level must be higher than TiO_2(ETL) layer to avoid electron recombination in the region [98]. Similarly, the $CsPbI_2Br$ valence-band level should be aligned at lower than Cu_2O(HTL). Moreover, the built potentials at the $CsPbI_2Br/TiO_2$ and $CsPbI_2Br/Cu_2O$(HTL) interfaces are responsible for the charge carrier collections at the two sides.

It should be noted that in both separate bottom sub-cell and tandem cell, the optimal CZTSSe band gap 1.40 eV is matching well with the perovskite band gap 1.65 eV. Good matching between band gaps of perovskite and CZTSSe layers improves the performance of the structure. At higher band gap values, the cell efficiency, J_{SC} and *FF* decrease, Fig. 8a–f. This is understandable as wider band gaps limit photon absorption and lower charge carrier generation, which affects J_{SC} and consequently the efficiency. V_{OC} is not strongly affected as observed from Fig. 8g and h. That is because the built-in potential increases with band gap values.

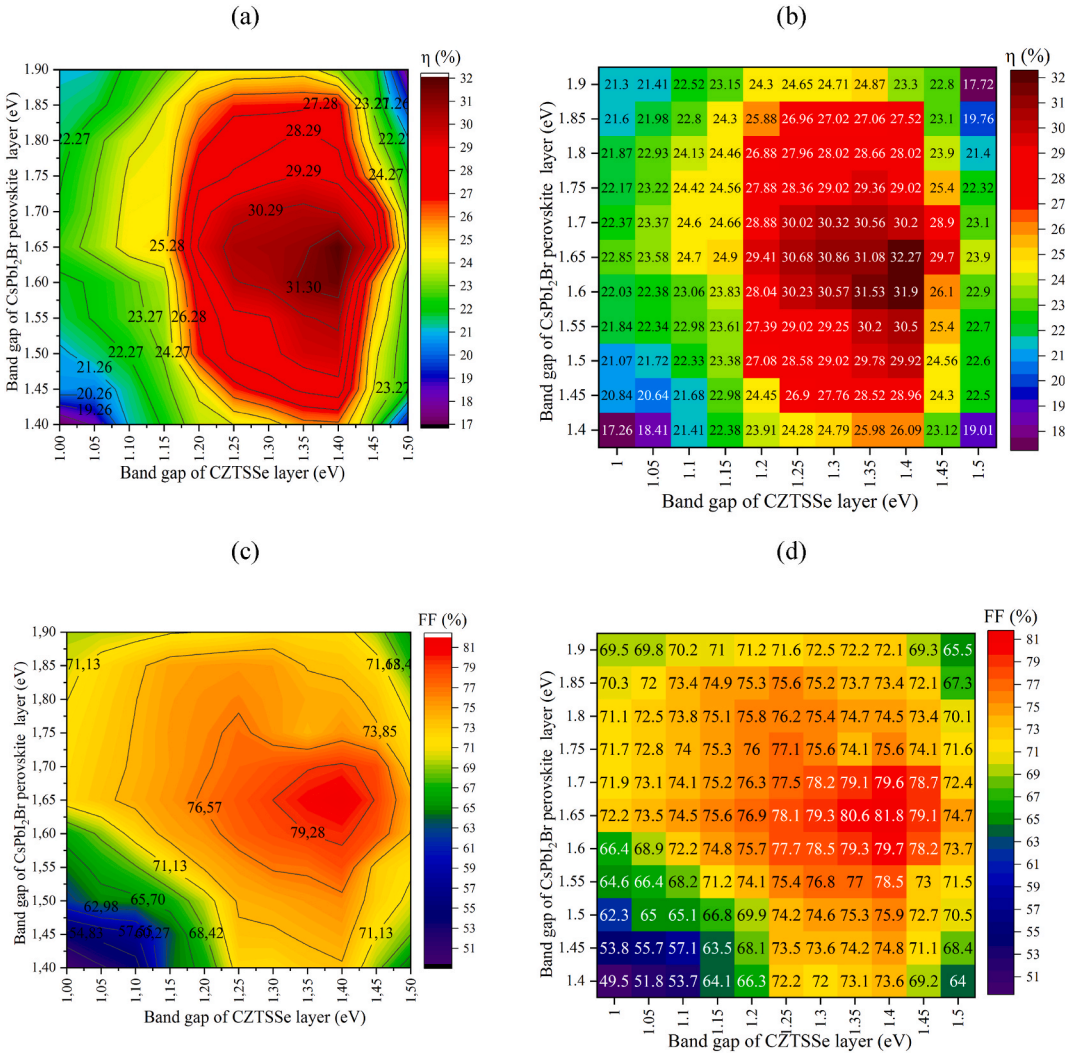

Fig. 8. CZTSSe and $CsPbI_2Br$ band gap effects on tandem solar cell performance. (a) & (b) for η%, (c) & (d) *FF*%, (e) & (f) J_{SC}, (g) & (h) V_{OC}.

3.2.3. CZTSSe and $CsPbI_2Br$ perovskite doping concentration effects

Effects of doping concentrations of both CZTSSe and perovskite layers have been studied. The doping concentration is responsible for transportation of charge carriers and electrical conductivity in the semiconductor material. The doping concentrations have been varied here in the ranges 10^{13} -10^{17} and 10^{15} - 10^{18} cm^{-3} for the perovskite and CZTSSe layers, respectively, Fig. 9. Other parameters have been kept fixed.

Fig. 9 shows that with increased doping concentrations the tandem cell characteristics are improved. With higher doping concentrations, the semiconductors have higher conductivity which allows higher photocurrent [99]. The highest tandem cell characteristics are observed at optimal doping concentrations 1×10^{17} and 1×10^{15} cm^{-3} for CZTSSe and perovskite, respectively. At these concentrations, the efficiency and *FF* maximum values are 32.41 % and 79.89 % respectively, while J_{SC} and V_{OC} assume maximum values of 37 mA/cm^2 and 1.82 V, as observed from Fig. 9a–h.

At concentrations lower or higher than these (optimal) concentrations, cell performance decreases. Therefore, increased doping concentration has two opposing effects, as it may increase or lower performance. Similar behaviors were also earlier reported [99]. At doping concentrations other than the optimal ones, there is a decrease in motilities leading to increased recombination centers at the interfaces $TiO_2/CsPbI_2Br$, $Cu_2O/CsPbI_2Br$, CdS/CZTSSe and CZTSSe/CdS. Moreover, too high concentrations create crystal defects and electron traps that further lower cell performance.

The cell performance is also greatly affected by the ETL conduction band offset (between ETL and absorption layers, and by defect density at the interface. As known, the ETL/perovskite ($TiO_2/CsPbI_2Br$) are of different types and lead to the creation of the junction. This is due to the resulting electric field that controls the carrier transfer to the two contacts. It may also lead to recombination in this zone, especially if the ETL layer is not carefully chosen in terms of band gap value. Therefore, the band gap must be suitable for the

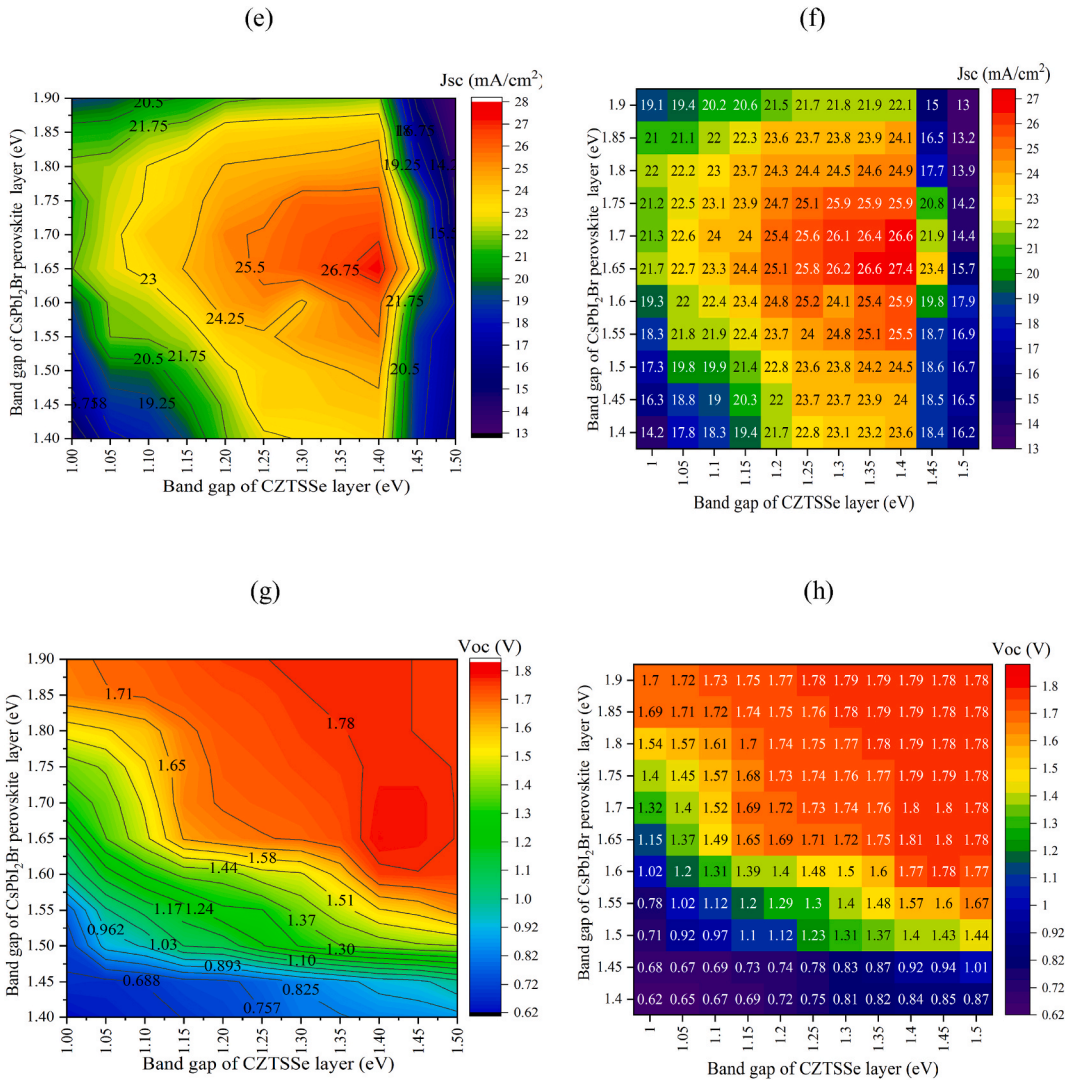

Fig. 8. (*continued*).

perovskite, to facilitate the electron carrier free passage. The perovskite conduction band level must be higher than the ETL layer conduction band. Moreover, the ETL, perovskite and HTL materials must be stable to heat and humidity to yield durable tandem solar cells [100].

3.3. Tandem cell vs. separate sub-cell comparison

Fig. 10 shows that the top sub-cell, with the relatively wide-band gap $CsPbI_2Br$ perovskite, exhibits higher V_{OC} (1.06 V) but smaller J_{SC} (27.4 mA/cm^2). With a relatively wide band gap, the low J_{SC} is expected as shorter wavelength photons are only involved, while the V_{OC} value is increased. All other longer wavelength photons go through to the CZTSSe and Si bi-absorber layer. The bottom sub-cell, exhibits high J_{SC} 37.18 mA/cm^2 and low V_{OC} 0.746 V. This is expected from the relatively narrow band gap value for the bi-absorber layer. Table 4 summarizes these results.

As per the tandem solar cell, entries # 2 and 3 in Table 4 show that the J_{SC} value (27.79 mA/cm^2) resembles the low value for the top sub-cell. This is understandable as the two sub-cells are connected in series, where the lower current determines the total current, as discussed in Section III.2.a above.

Table 4 also shows that the V_{OC} value (1.81 V) for the tandem cell approximately equals the summation of V_{OC} values for the bottom and the top sub-cells combined, entries # 1–3. Again, this is due to the serial connection of the two sub-cells together in the tandem cell.

Despite the fact that the tandem cell shows lower J_{SC} than the bottom sub-cell separately, the overall conversion efficiency for the former is much higher. The much higher V_{OC} in the tandem solar cell makes up for its relatively low J_{SC}. Table 4, entries # 1–3, show

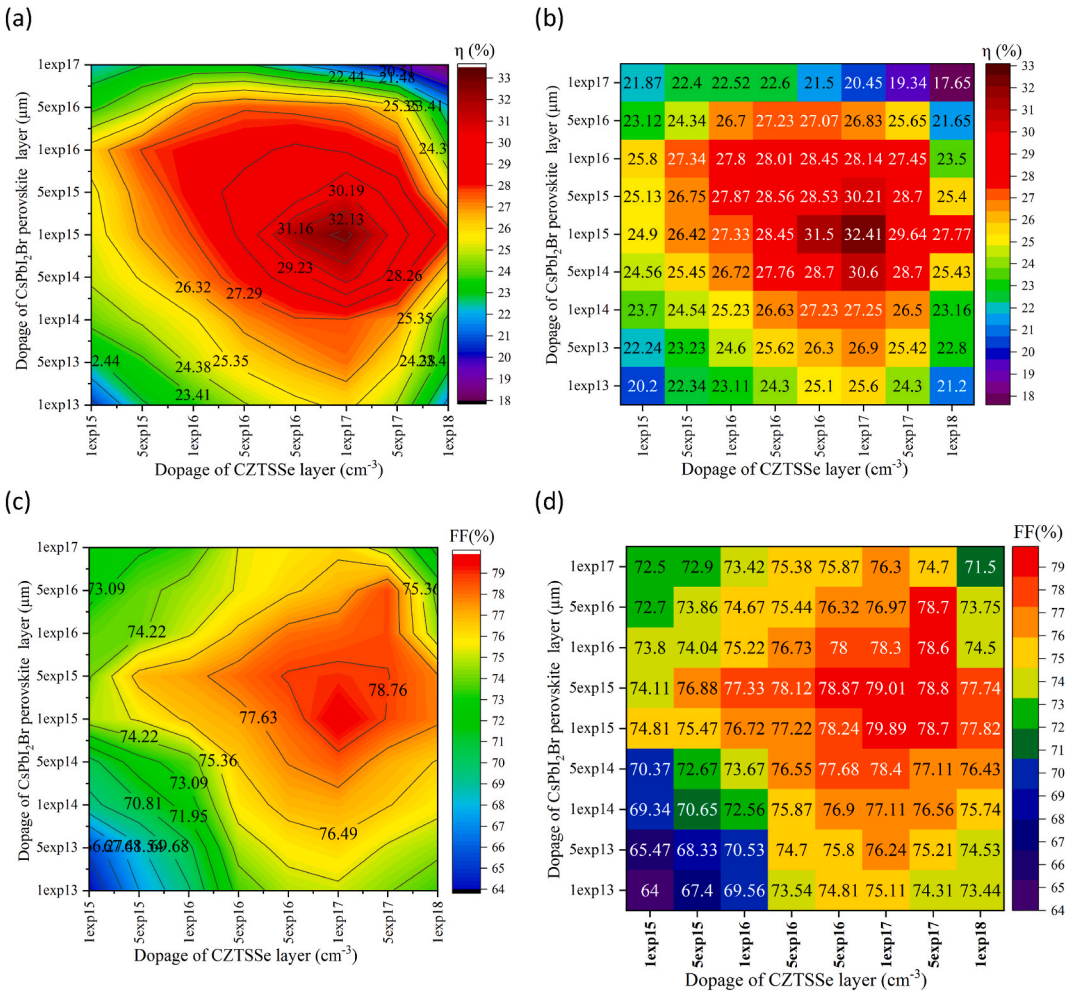

Fig. 9. CZTSSe and $CsPbI_2Br$ doping concentration effects on tandem cell characteristics. (a) & (b) for η%, (c) & (d) *FF*%, (e) & (f) J_{SC}, (g) & (h) V_{OC}.

that the tandem-cell conversion efficiency value approximately resembles the sum of values for the separate sub-cells.

Comparison of entry # 3 with entry # 5, shows that the inclusion of Si in the bottom sub-cell gives improvement in J_{SC}, V_{OC} and efficiency, despite that the reference used a four-terminal tandem cell. Inclusion of Si in the CZTSSe/Si double absorber layer allow absorption of photons with a wider wavelength range. Comparison with earlier systems, those including CIGS layers (entries # 6,7 and 8) shows the that the present tandem solar cell has higher conversion efficiency while using the safe, abundant elements in the CZTSSe layer.

The findings underscore the practical value of combining the CZTSSe/Si bottom sub-cell, with the top $CsPbI_2Br$ perovskite sub-cell, in tandem solar cell design. A highly efficient tandem cell has been constructed by combining the two sub-cells, on the condition that their layer thicknesses and band gaps are optimized and aligned together. The synergistic effect of these optimized parameters and materials yields a substantial enhancement in solar cell efficiency, opening up new possibilities for the development of highly efficient and sustainable energy technologies.

4. Conclusion

A novel tandem-solar cell structure is proposed here by simulation using the SCAPS numerical simulation software. The tandem cell configuration involves two sub-cells. The bottom sub-cell, Al–ZnO/i-ZnO/n-CdS/p-CZTSSe/p-Si, has been optimized in layer thickness, doping concentration and band gap. The optimized characteristics are: open-circuit potential 0.742 V, short-circuit current density 37.18 mA/cm^2, fill factor 85.03 % and overall efficiency 20.94 %. The optimal bottom sub-cell parameters have been used in the tandem-solar cell that involves the top sub-cell $TiO_2/CsPbI_2Br/Cu_2O$, utilizing parameters obtained from experimental results (Supplementary materials) and earlier studies. The optimized tandem-solar cell exhibits a high efficiency of over 32.41 %, with a fill factor of 79.89 %. Based on the present results, it is highly recommended to do more simulation and experimental study on tandem solar cells

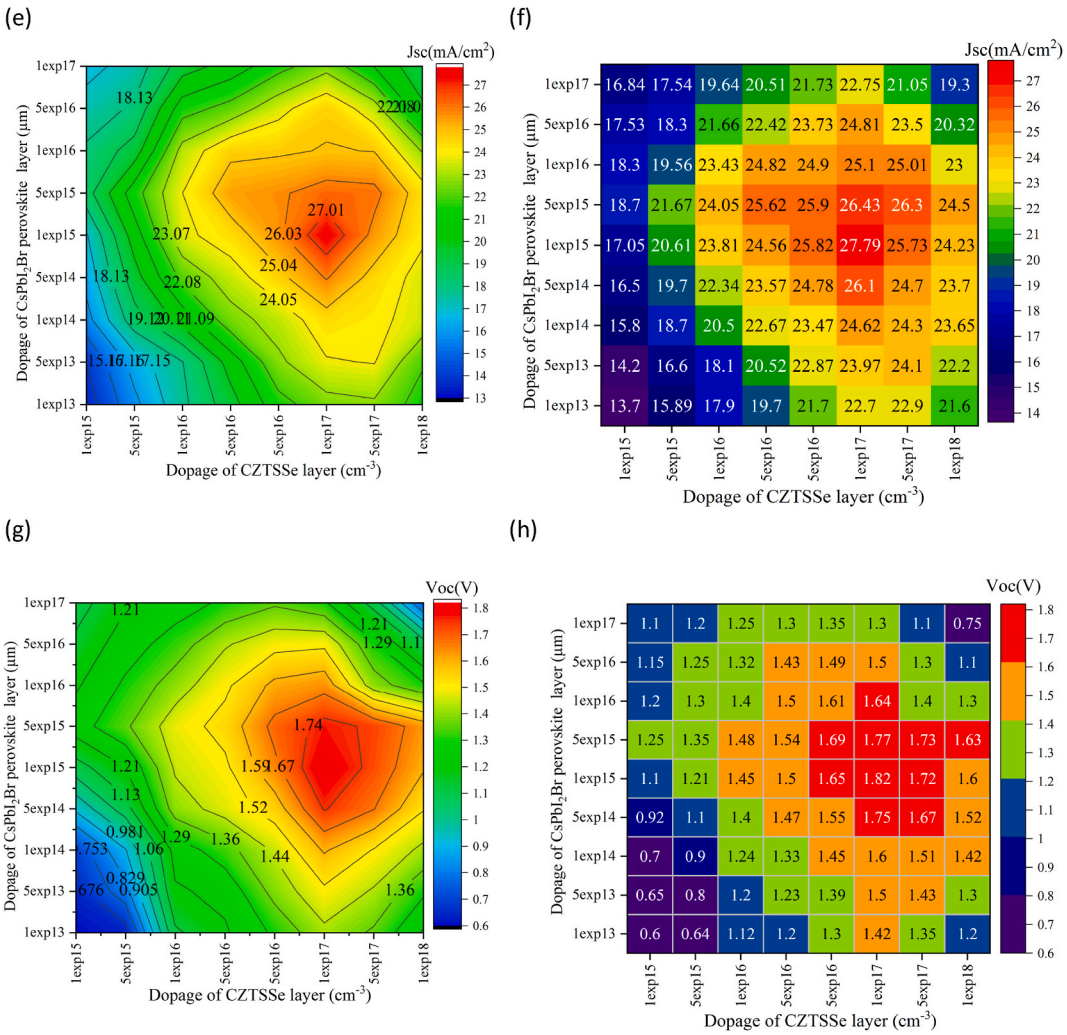

Fig. 9. (*continued*).

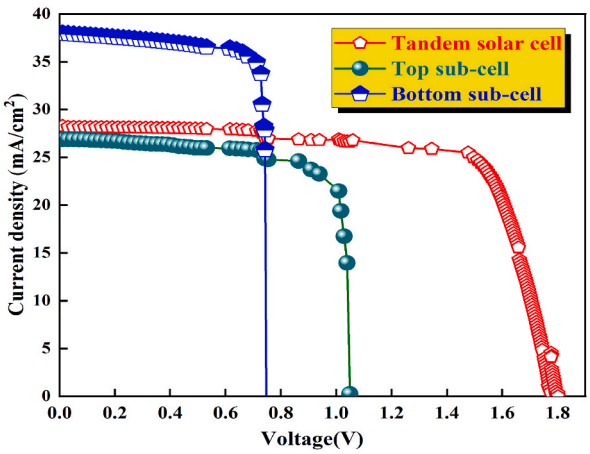

Fig. 10. Simulated *J-V* plots for bottom and top sub-cells, together with the proposed tandem cell.

that involve safe and low-cost double absorber layers such as CZTSSe/Si.

CRediT authorship contribution statement

Naceur Selmane: Writing – review & editing, Writing – original draft, Software, Formal analysis, Data curation. **Ali Cheknane:** Supervision, Funding acquisition, Conceptualization. **Hikmat S. Hilal:** Writing – review & editing, Validation.

Declaration of competing interest

The authors declare that they have no known competing financial interests or personal relationships that could have appeared to influence the work reported in this paper.

Data availability

Data will be made available on request.

Acknowledgment

All authors express thanks to Professor Marc Burgelman, of Gent University, Belgium, for kind help with software. Naceur Selmane and Ali Cheknane acknowledge support from Amar Telidji University-Laghouat, PRFU Project # A10N01UN030120220002, under the title: Contribution à l'étude des propriétés physico-chimiques des nouveaux matériaux: Applications dans le domaine des énergies renouvelables. Thanks are also due to General Directorate of Scientific Research & Technological Development- DGRSDT-, Algeria. Hikmat S. Hilal thanks An-Najah N. University for technical help.

Appendix A. Supplementary data

Supplementary data to this article can be found online at https://doi.org/10.1016/j.micrna.2024.207940.

References

[1] S. Hänni, G. Bugnon, G. Parascandolo, M. Boccard, J. Escarré, M. Despeisse, F. Meillaud, C. Ballif, High-efficiency microcrystalline silicon single-junction solar cells, Prog. Photovoltaics Res. Appl. 21 (2013) 821–826.
[2] R.M. Geisthardt, M. Topič, J.R. Sites, Status and potential of CdTe solar-cell efficiency, IEEE J. Photovoltaics 5 (2015) 1217–1221.
[3] F. Goucher, G. Pearson, M. Sparks, G. Teal, W. Shockley, Theory and experiment for a Germanium p– n junction, Phys. Rev. 81 (1951) 637.
[4] C. Battaglia, A. Cuevas, S. De Wolf, High-efficiency crystalline silicon solar cells: status and perspectives, Energy Environ. Sci. 9 (2016) 1552–1576.
[5] Y. Liu, Y. Li, Y. Wu, G. Yang, L. Mazzarella, P. Procel-Moya, A.C. Tamboli, K. Weber, M. Boccard, O. Isabella, High-efficiency silicon heterojunction solar cells: materials, devices and applications, Mater. Sci. Eng. R Rep. 142 (2020) 100579.
[6] M.M.A. Moon, M.F. Rahman, J. Hossain, A.B.M. Ismail, Comparative study of the second generation a-Si: H, CdTe, and CIGS thin-film solar cells, Adv. Mater. Res. 1154 (2019) 102–111.
[7] J.Y. Kim, J.-W. Lee, H.S. Jung, H. Shin, N.-G. Park, High-efficiency perovskite solar cells, Chem. Rev. 120 (2020) 7867–7918.
[8] N.S. Kumar, K.C.B. Naidu, A review on perovskite solar cells (PSCs), materials and applications, Journal of Materiomics 7 (2021) 940–956.
[9] H. Bencherif, F. Meddour, M. Elshorbagy, M.K. Hossain, A. Cuadrado, M.A. Abdi, T. Bendib, S. Kouda, J. Alda, Performance enhancement of (FAPbI 3) 1-x (MAPbBr 3) x perovskite solar cell with an optimized design, Micro and Nanostructures 171 (2022) 207403.
[10] K. Dey, B. Roose, S.D. Stranks, Optoelectronic properties of low-bandgap halide perovskites for solar cell applications, Adv. Mater. 33 (2021) 2102300.
[11] S. Valsalakumar, A. Roy, T.K. Mallick, J. Hinshelwood, S. Sundaram, An overview of current printing technologies for large-scale perovskite solar cell development, Energies 16 (2022) 190.
[12] N. Li, X. Niu, Q. Chen, H. Zhou, Towards commercialization: the operational stability of perovskite solar cells, Chem. Soc. Rev. 49 (2020) 8235–8286.
[13] J. Huang, D. Zhou, H. Yan, C. Meng, Y. Yang, J. Liu, M. Wang, P. Xu, Z. Peng, J. Chen, A multiple-coordination framework for CsPbI 2 Br perovskite solar cells, J. Mater. Chem. C 12 (2024) 4112–4122.
[14] Y. Dong, J. Duan, D. Luo, J. Liu, X. Wang, X. Liu, Z. Huang, X. Li, Y. Gao, Interface optimization of CsPbI2Br based perovskite solar cells by device simulation, Mater. Today Commun. 39 (2024) 108695.
[15] J. Song, H. Xie, E.L. Lim, A. Hagfeldt, D. Bi, Progress and perspective on inorganic CsPbI2Br perovskite solar cells, Adv. Energy Mater. 12 (2022) 2201854.
[16] S. Wang, Y. Peng, L. Li, Z. Zhou, Z. Liu, S. Zhou, M. Yao, Impact of loss mechanisms on performances of perovskite solar cells, Phys. B Condens. Matter 647 (2022) 414363.
[17] B. Ehrler, E. Alarcón-Lladó, S.W. Tabernig, T. Veeken, E.C. Garnett, A. Polman, Photovoltaics Reaching for the Shockley–Queisser Limit, ACS Publications, 2020.
[18] A.R. Zanatta, The Shockley–Queisser Limit and the Conversion Efficiency of Silicon-Based Solar Cells, Results in Optics, vol. 9, 2022 100320.
[19] J. Kim, S. Lee, S. Park, M. Ju, Y. Kim, E.-C. Cho, S.K. Dhungel, J. Yi, Highly efficient bifacial silicon/silicon tandem solar cells, IEEE Access 11 (2023) 21326–21331.
[20] R. Lin, J. Xu, M. Wei, Y. Wang, Z. Qin, Z. Liu, J. Wu, K. Xiao, B. Chen, S.M. Park, All-perovskite tandem solar cells with improved grain surface passivation, Nature 603 (2022) 73–78.
[21] M.A. Shafi, L. Khan, S. Ullah, M.Y. Shafi, A. Bouich, H. Ullah, B. Mari, Novel compositional engineering for~ 26% efficient CZTS-perovskite tandem solar cell, Optik 253 (2022) 168568.
[22] A. Maoucha, F. Djeffal, H. Ferhati, F. AbdelMalek, Eco-friendly perovskite/CZTSSe tandem cell exceeding 28% efficiency through current matching and bandgap optimization: a numerical investigation, The European Physical Journal Plus 138 (2023) 620.
[23] A. Maoucha, F. Djeffal, H. Ferhati, SCAPS-FDTD simulation of 20.1% efficient Perovskite-SnS tandem solar cell based on alternative charge transport layers and Au-nanoparticles, Phys. Scripta 99 (2023) 015919.

[24] C. Wang, Y. Zhao, T. Ma, Y. An, R. He, J. Zhu, C. Chen, S. Ren, F. Fu, D. Zhao, A universal close-space annealing strategy towards high-quality perovskite absorbers enabling efficient all-perovskite tandem solar cells, Nat. Energy 7 (2022) 744–753.
[25] S. Yang, J. Wen, Z. Liu, Y. Che, J. Xu, J. Wang, D. Xu, N. Yuan, J. Ding, Y. Duan, A key 2D intermediate phase for stable high-efficiency CsPbI2Br perovskite solar cells, Adv. Energy Mater. 12 (2022) 2103019.
[26] B. Kim, K.-I. Ryu, S.-G. Ko, K.-S. Sonu, J.-H. Ri, H.-S. So, C.-I. So, Y.-S. Kim, C.-J. Yu, Performance improvement of hole-transport material-free mesoporous perovskite solar cells with carbon electrodes using a solid–gas reaction, ACS Appl. Energy Mater. 4 (2021) 6606–6615.
[27] M. Park, S.C. Hong, Y.-W. Jang, J. Byeon, J. Jang, M. Han, U. Kim, K. Jeong, M. Choi, G. Lee, Scalable production of high performance flexible perovskite solar cells via film-growth-megasonic-spray-coating system, International Journal of Precision Engineering and Manufacturing-Green Technology 10 (2023) 1223–1234.
[28] Y. Li, N. Liu, Z. Xu, Z. Xu, Y. Pan, J. Zhang, L. Huang, Z. Hu, Y. Zhu, X. Liu, Doping engineering of ZnO electron transporting layer for high performance CsPbI2Br inorganic perovskite solar cells, Appl. Phys. Lett. 123 (2023).
[29] G. Tseberlidis, C. Gobbo, V. Trifiletti, V. Di Palma, S. Binetti, Cd-free kesterite solar cells: state-of-the-art and perspectives, Sustainable Materials and Technologies (2024) e01003.
[30] S.K. Hwang, S.J. Park, J.H. Park, J.H. Yoon, J. Yu Cho, D.K. Cho, J. Heo, G.Y. Kim, J.Y. Kim, Cs-treatments in kesterite thin-film solar cells for efficient perovskite tandems (small 16/2024), Small 20 (2024) 2470123.
[31] D. Wang, S. Yao, Y. Zhong, L. Peng, T. Shi, J. Chen, X. Liu, J. Lin, Optoelectronic simulation of a four-terminal all-inorganic CsPbI 3/CZTSSe tandem solar cell with high power conversion efficiency, Phys. Chem. Chem. Phys. 24 (2022) 22746–22755.
[32] T. AlZoubi, A. Moghrabi, M. Moustafa, S. Yasin, Efficiency boost of CZTS solar cells based on double-absorber architecture: device modeling and analysis, Sol. Energy 225 (2021) 44–52.
[33] E. Emon, A. Islam, M. Sobayel, S. Islam, M. Akhtaruzzaman, N. Amin, A. Ahmed, M. Rashid, A comprehensive photovoltaic study on tungsten disulfide (WS2) buffer layer based CdTe solar cell, Heliyon 9 (2023) e14438.
[34] M. Kumar, S. Kumar, 24.13% efficient TiO2/i–a–Si: H/p–c–Si heterojunction solar cell by AFORS-HET numerical simulation, Opt. Quant. Electron. 55 (2023) 441.
[35] T.I. Alanazi, O.I. Eid, M. Okil, Numerical study of flexible perovskite/Si tandem solar cell using TCAD simulation, Opt. Quant. Electron. 55 (2023) 1152.
[36] B. Gopal Krishna, D.S. Ghosh, S. Tiwari, Device simulation of perovskite/silicon tandem solar cell with antireflective coating, Opt. Quant. Electron. 55 (2023) 197.
[37] N.E.I. Boukortt, S. Patanè, A.M. AlAmri, D. AlAjmi, K. Bulayyan, N. AlMutairi, Numerical investigation of perovskite and u-CIGS based tandem solar cells using Silvaco TCAD simulation, Silicon 15 (2023) 293–303.
[38] M. Okil, A. Shaker, M.M. Salah, T.M. Abdolkader, I.S. Ahmed, Investigation of polymer/Si thin film tandem solar cell using TCAD numerical simulation, Polymers 15 (2023) 2049.
[39] K.G. Beepat, D.P. Sharma, D. Pathak, A. Mahajan, COMSOL multiphysics-based modeling approach to solar cell development, Int. J. Mod. Phys. B 37 (2023) 2350114.
[40] E.T. Mohamed, A.O. Maka, M. Mehmood, A.M. Direedar, N. Amin, Performance simulation of single and dual-junction GaInP/GaAs tandem solar cells using AMPS-1D, Sustain. Energy Technol. Assessments 44 (2021) 101067.
[41] S.S. Bal, A. Basak, U.P. Singh, Numerical modeling and performance analysis of Sb-based tandem solar cell structure using SCAPS–1D, Opt. Mater. 127 (2022) 112282.
[42] F. Jafarzadeh, H. Aghili, H. Nikbakht, S. Javadpour, Design and optimization of highly efficient perovskite/homojunction SnS tandem solar cells using SCAPS-1D, Sol. Energy 236 (2022) 195–205.
[43] M. Abderrezek, M.E. Djeghlal, Numerical study of CZTS/CZTSSe tandem thin film solar cell using SCAPS-1D, Optik 242 (2021) 167320.
[44] J. Zhang, B. Yao, Z. Ding, Y. Li, T. Wang, C. Wang, D. Ma, D. Zhang, Efficiency enhancement of Cu2ZnSn (S, Se) 4 solar cells by addition a CuSe intermediate layer between Cu2ZnSn (S, Se) 4 and Mo electrode, J. Alloys Compd. 911 (2022) 165056.
[45] M.K. Mohammed, A.K. Al-Mousoi, A. Kumar, M.M. Sabugaa, R. Seemaladinne, R. Pandey, J. Madan, M.K. Hossain, B.S. Goud, A.A. Al-Kahtani, Harnessing the potential of Dion-Jacobson perovskite solar cells: insights from SCAPS simulation techniques, J. Alloys Compd. 963 (2023) 171246.
[46] S.K. Tummala, P. Harishitha, B. Pravallika, S. Alekya, M. Mamatha, Performance analysis of c-Si & CdS solar cells, Mater. Today: Proc. (2023), https://doi.org/10.1016/j.matpr.2023.06.373.
[47] A. Bosio, G. Rosa, N. Romeo, Past, present and future of the thin film CdTe/CdS solar cells, Sol. Energy 175 (2018) 31–43.
[48] J. Melchor-Robles, K. Nieto-Zepeda, N. Vázquez-Barragán, M. Arreguín-Campos, K. Rodríguez-Rosales, J. Cruz-Gómez, A. Guillén-Cervantes, J. Santos-Cruz, M. d.l.L. Olvera, G. Contreras-Puente, Characterization of CdS/CdTe ultrathin-film solar cells with different CdS thin-film thicknesses obtained by RF sputtering, Coatings 14 (2024) 452.
[49] M. Sbeah, A. Zyoud, M. Ishteiwi, M. Hajjyahya, N. Al Armouzi, N. Qamhieh, A.R. Hajamohideen, S. Zyoud, H.H. Helal, H. Bsharat, Assessment of flexible pristine CdS film electrodes in photoelectrochemical light-to-electricity conversions, Mater. Chem. Phys. 293 (2023) 126967.
[50] A. Zyoud, S.A. Alrob, T.W. Kim, H.-J. Choi, M.H. Helal, H. Bsharat, H.S. Hilal, Electrochemically and chemically deposited polycrystalline CdSe electrodes with high photoelectrochemical performance by recycling from waste films, Mater. Sci. Semicond. Process. 107 (2020) 104852.
[51] K.T. Arockiya Dass, M.K. Hossain, L. Marasamy, Highly efficient emerging Ag2BaTiSe4 solar cells using a new class of alkaline earth metal-based chalcogenide buffers alternative to CdS, Sci. Rep. 14 (2024) 1473.
[52] A. Cherouana, R. Labbani, Study of CZTS and CZTSSe solar cells for buffer layers selection, Appl. Surf. Sci. 424 (2017) 251–255.
[53] H. Ferhati, T. Berghout, F. Djeffal, Efficient SnS solar cells via plasmonic light trapping and alternative buffer layers: a combined machine learning and fdtd analysis, Plasmonics (2024) 1–11.
[54] N. Selmane, A. Cheknane, N. Gabouze, N. Maloufi, M. Aillerie, Experimental study of optical and electrical properties of ZnO nano composites electrodeposited on n-porous silicon substrate for photovoltaic applications, in: E3S Web of Conferences, EDP Sciences, 2017 00155.
[55] N. Selmane, A. Cheknane, M. Aillerie, H.S. Hilal, Effect of ZnO-based TCO on the performance of a-Si H (n)/a-Si H (i)/c-Si H (p)/Al BSF (p+)/Al heterojunction solar cells, Environ. Prog. Sustain. Energy 38 (2019) 13114.
[56] D. Roy, M. Basu, S. Paul, Synthesis of Al-doped zinc oxide nano particle TCO material by simple Sol-Gel method, in: Journal of Physics: Conference Series, IOP Publishing, 2020 012007.
[57] B. Srujana, A. Prakash, S. Chattopadhyay, M. Mahesha, Zirconium doped zinc oxide thin films grown by spray pyrolysis technique for TCO applications, Mater. Today Commun. 37 (2023) 107476.
[58] N. Selmane, A. Cheknane, H.S. Hilal, Optimization of Al-doped ZnO transparent conducting oxide and emitter layers for enhanced performance of Si heterojunction solar cells, J. Electron. Mater. 49 (2020) 2179–2190.
[59] J. Pilz, A. Perrotta, G. Leising, A.M. Coclite, ZnO thin films grown by plasma-enhanced atomic layer deposition: material properties within and outside the "atomic layer deposition window", Phys. Status Solidi 217 (2020) 1900256.
[60] B.A. Ünlü, D. Sener, S. Tekin, E.A. Yildiz, A. Karatay, T. Serin, A. Elmali, Enhancement of nonlinear absorption in defect controlled ZnO polycrystalline thin films by means of Co-doping, Phys. Status Solidi 258 (2021) 2000539.
[61] V. Privezentsev, A. Sergeev, A. Firsov, E. Yakimov, D. Irzhak, Structure and properties of nanostructured SZO films obtained by electron-beam evaporation, Crystallogr. Rep. 66 (2021) 1090–1094.
[62] S. Ullah, F. Ahmed, A. Badshah, A. Ali Altaf, R. Raza, B. Lal, R. Hussain, Solvothermal preparation of ZnO nanorods as anode material for improved cycle life Zn/AgO batteries, PLoS One 8 (2013) e75999.
[63] P.M. Radingoana, S. Guillemet-Fritsch, J. Noudem, P.A. Olubambi, G. Chevallier, C. Estournès, Microstructure and thermoelectric properties of Al-doped ZnO ceramic prepared by spark plasma sintering, J. Eur. Ceram. Soc. 43 (2023) 1009–1016.

[64] N. Selmane, A. Cheknane, F. Khemloul, M.H. Helal, H.S. Hilal, Cost-saving and performance-enhancement of CuInGaSe solar cells by adding CuZnSnSe as a second absorber, Sol. Energy 234 (2022) 64–80.
[65] S. Ahmmed, A. Aktar, M.F. Rahman, J. Hossain, A.B.M. Ismail, A numerical simulation of high efficiency CdS/CdTe based solar cell using NiO HTL and ZnO TCO, Optik 223 (2020) 165625.
[66] M.F. Rahman, M.M.A. Moon, M.K. Hossain, M.H. Ali, M.D. Haque, A. Kuddus, J. Hossain, A.B.M. Ismail, Concurrent investigation of antimony chalcogenide (Sb2Se3 and Sb2S3)-based solar cells with a potential WS2 electron transport layer, Heliyon 8 (2022) e12034.
[67] M.F. Rahman, M.K. Hasan, M. Chowdhury, M.R. Islam, M.H. Rahman, M.A. Rahman, S.R. Al Ahmed, A.B.M. Ismail, M. Amami, M.K. Hossain, A qualitative design and optimization of CIGS-based solar cells with Sn2S3 back surface field: a plan for achieving 21.83% efficiency, Heliyon 9 (2023) e22866.
[68] M.S. Reza, M.F. Rahman, A. Kuddus, M.K. Mohammed, A.K. Al-Mousoi, M.R. Islam, A. Ghosh, S. Bhattarai, R. Pandey, J. Madan, Boosting efficiency above 28% using effective charge transport layer with Sr 3 SbI 3 based novel inorganic perovskite, RSC Adv. 13 (2023) 31330–31345.
[69] M.E. Islam, M.R. Islam, S. Ahmmed, M.K. Hossain, M.F. Rahman, Highly efficient SnS-based inverted planar heterojunction solar cell with ZnO ETL, Phys. Scripta 98 (2023) 065501.
[70] M.K. Hossain, D. Samajdar, R.C. Das, A. Arnab, M.F. Rahman, M. Rubel, M.R. Islam, H. Bencherif, R. Pandey, J. Madan, Design and simulation of Cs2BiAgI6 double perovskite solar cells with different electron transport layers for efficiency enhancement, Energy & Fuels 37 (2023) 3957–3979.
[71] M.F. Rahman, N. Mahmud, I. Alam, Design and Numerical Analysis of CIGS-Based Solar Cell with V, 2023.
[72] A. Solon, J.M. Horowitz, On the Einstein relation between mobility and diffusion coefficient in an active bath, J. Phys. Math. Theor. 55 (2022) 184002.
[73] J. Spiechowicz, I.G. Marchenko, P. Hänggi, J. Łuczka, Diffusion coefficient of a Brownian particle in equilibrium and nonequilibrium: Einstein model and beyond, Entropy 25 (2022) 42.
[74] A. Raj, M. Kumar, A. Kumar, A. Laref, K. Singh, S. Sharma, A. Anshul, Effect of doping engineering in TiO2 electron transport layer on photovoltaic performance of perovskite solar cells, Mater. Lett. 313 (2022) 131692.
[75] M. Hasan, S.M. Sultana, S.J. Papiya, N.A. Salsabil, Z. Musarrat, S.M. Tuba, M.F. Nayan, Impact of absorber layer thickness and defect density on the performance of MAPbI3 solar cells based on CuO2 as hole transport material, Engineering Research Express 5 (2023) 035080.
[76] O. Baka, A. Azizi, S. Velumani, G. Schmerber, A. Dinia, Effect of Al concentrations on the electrodeposition and properties of transparent Al-doped ZnO thin films, J. Mater. Sci. Mater. Electron. 25 (2014) 1761–1769.
[77] S. Sudjatmoko, W. Wirjoadi, B. Siswanto, Influence of substrate temperature on structural, electrical and optical properties of ZnO: Al thin films, At. Indones. 35 (2009) 115–125.
[78] Y. Zhao, B. Chen, A. Miner, S. Priya, Low thermal conductivity of Al-doped ZnO with layered and correlated grains, RSC Adv. 4 (2014) 18370–18377.
[79] A. Ghosh, S. Karmakar, F.A. Rahimi, R.S. Roy, S. Nath, U.K. Gautam, T.K. Maji, Confinement matters: stabilization of CdS nanoparticles inside a postmodified MOF toward photocatalytic hydrogen evolution, ACS Appl. Mater. Interfaces 14 (2022) 25220–25231.
[80] M. Rahman, S. Islam, A. Khandaker, T. Hossain, M. Rashid, Bilayer CZTS/Si absorber for obtaining highly efficient CZTS solar cell, Sol. Energy 230 (2021) 1189–1198.
[81] S.K. Hwang, I.J. Park, S.W. Seo, J.H. Park, S.J. Park, J.Y. Kim, Electrochemically deposited CZTSSe thin films for monolithic perovskite tandem solar cells with efficiencies over 17, Energy & Environmental Materials 7 (2024) e12489.
[82] C. Pinzón, N. Martínez, G. Casas, F.C. Alvira, N. Denon, G. Brusasco, H. Medina Chanduví, A.V. Gil Rebaza, M.A. Cappelletti, Optimization of inverted all-inorganic CsPbI3 and CsPbI2Br perovskite solar cells by SCAPS-1D simulation, in: Solar, MDPI, 2022, pp. 559–571.
[83] X. Wu, F.E. Oropeza, Z. Qi, M. Einert, C. Tian, C. Maheu, K. Lv, J.P. Hofmann, Influence of Mo doping on interfacial charge carrier dynamics in photoelectrochemical water oxidation on BiVO 4, Sustain. Energy Fuels 7 (2023) 2923–2933.
[84] C.A. Benisha, S. Routray, Performance enhancement of kesterite solar cell with doped-silicon back surface field layer, Silicon 14 (2022) 8045–8054.
[85] D. Yu, Q. Wei, H. Li, J. Xie, X. Jiang, T. Pan, H. Wang, M. Pan, W. Zhou, W. Liu, Quasi-2D bilayer surface passivation for high efficiency narrow bandgap perovskite solar cells, Angew. Chem. 134 (2022) e202202346.
[86] H.-T. Liu, Q. Sun, Y. Zhong, Q. Deng, L. Gan, F.-L. Lv, X.-L. Shi, Z.-G. Chen, R. Ang, High-performance in n-type PbTe-based thermoelectric materials achieved by synergistically dynamic doping and energy filtering, Nano Energy 91 (2022) 106706.
[87] S. Jamil, U. Saha, M.K. Alam, Surface plasmon enhanced ultrathin Cu 2 ZnSnS 4/crystalline-Si tandem solar cells, Nanoscale Adv. 5 (2023) 2887–2896.
[88] V. Shukla, G. Panda, The performance study of CdTe/CdS/SnO2 solar cell, Mater. Today: Proc. 26 (2020) 487–491.
[89] K.R. Ngoy, A.K. Singh, T.-C. Jen, A.M. Ali, Numerical analysis of thin film Cu2InGaSe4 solar cells design, Sol. Energy 225 (2021) 53–59.
[90] D.A. Fentahun, A. Tyagi, K.K. Kar, Numerically investigating the AZO/Cu2O heterojunction solar cell using ZnO/CdS buffer layer, Optik 228 (2021) 166228.
[91] M.F. Rahman, M. Habib, M.H. Ali, M. Rubel, M.R. Islam, A.B. Md Ismail, M.K. Hossain, Design and numerical investigation of cadmium telluride (CdTe) and iron silicide (FeSi2) based double absorber solar cells to enhance power conversion efficiency, AIP Adv. 12 (2022).
[92] E. Raza, Z. Ahmad, M. Asif, F. Aziz, K. Riaz, M.Q. Mehmood, J. Bhadra, N.J. Al-Thani, Numerical modeling and performance optimization of carbon-based hole transport layer free perovskite solar cells, Opt. Mater. 125 (2022) 112075.
[93] P. Kumar, S. Thokala, S.P. Singh, R. Singh, Research progress and challenges in extending the infra-red absorption of perovskite tandem solar cells, Nano Energy (2023) 109175.
[94] S.K. Hwang, I.J. Park, S.W. Seo, J.H. Park, S.J. Park, J.Y. Kim, Electrochemically deposited CZTSSe thin films for monolithic perovskite tandem solar cells with efficiencies over 17, Energy & Environmental Materials (2023) e12489.
[95] S. Shukla, M. Sood, D. Adeleye, S. Peedle, G. Kusch, D. Dahliah, M. Melchiorre, G.M. Rignanese, G. Hautier, R. Oliver, Over 15% efficient wide-band-gap Cu (In, Ga) S2 solar cell: suppressing bulk and interface recombination through composition engineering, Joule 5 (2021) 1816–1831.
[96] M. Mukherjee, R. Jana, A. Datta, Designing C 6 N 6/C 2 N van der Waals heterostructures for photogenerated charge carrier separation, Phys. Chem. Chem. Phys. 23 (2021) 3925–3933.
[97] H. Javaid, V.V. Duzhko, D. Venkataraman, Hole transport bilayer for highly efficient and stable inverted perovskite solar cells, ACS Appl. Energy Mater. 4 (2020) 72–80.
[98] M. Cheng, C. Zuo, Y. Wu, Z. Li, B. Xu, Y. Hua, L. Ding, Charge-transport layer engineering in perovskite solar cells, Sci. Bull. 65 (2020) 1237–1241.
[99] B. Zabelich, E. Nitiss, A. Stroganov, C.-S. Bres, Linear electro-optic effect in silicon nitride waveguides enabled by electric-field poling, ACS photonics 9 (2022) 3374–3383.
[100] N. Selmane, A. Cheknane, K.M. Gueddouda, F.A. Boukhelkhal, N. Baydogan, M.H. Helal, H.S. Hilal, RbGeI3/CuZnSnSSe/CuInGaSe/CdS tandem solar cell with improved performance and lowered cost, J. Mater. Sci. Mater. Electron. 35 (2024) 1109.
[101] M. Jost, E. Köhnen, A. Al-Ashouri, T. Bertram, S.p. Tomsic, A. Magomedov, E. Kasparavicius, T. Kodalle, B. Lipovsek, V. Getautis, Perovskite/CIGS tandem solar cells: from certified 24.2% toward 30% and beyond, ACS Energy Lett. 7 (2022) 1298–1307.
[102] N. Shrivastav, S. Kashyap, J. Madan, A.K. Al-Mousoi, M.K. Mohammed, M.K. Hossain, R. Pandey, J. Ramanujam, Perovskite-CIGS monolithic tandem solar cells with 29.7% efficiency: a numerical study, Energy & Fuels 37 (2023) 3083–3090.
[103] M. Hedayati, S. Olyaee, High-efficiency pn homojunction perovskite and CIGS tandem solar cell, Crystals 12 (2022) 703.
[104] Z. Khan, M. Noman, S.T. Jan, A.D. Khan, Systematic investigation of the impact of kesterite and zinc based charge transport layers on the device performance and optoelectronic properties of ecofriendly tin (Sn) based perovskite solar cells, Sol. Energy 257 (2023) 58–87.
[105] D. Jalalian, A. Ghadimi, A.K.S. Kaleh, Modeling and simulation of high-efficiency eco-friendly perovskite-CZTSe 1–x S x solar cell, Semiconductors 55 (2021) 373–378.